



## OPEN Microwave tomography for Lunar Penetrating Radar data processing in Chang'e 4 mission

Francesco Soldovieri<sup>1</sup>✉, Gianluca Gennarelli<sup>1</sup>, Yan Su<sup>2,3</sup>, Chunyu Ding<sup>4</sup> & Wei Du<sup>2,3</sup>

This work presents the results achieved by applying a microwave tomographic approach to the data collected by the Lunar Penetrating Radar onboard Yutu-2 rover in the frame of the Chang'e 4 mission. The adopted signal processing pipeline comprises two steps: the first one is a pre-processing stage involving time-domain procedures required to filter the clutter and noise on raw data; the second step regards the exploitation of a microwave tomographic approach designed to tackle the computational issue imposed by the large (in terms of probing wavelength) domain investigated by the rover. Two tomographic approaches, different for modeling the signal propagation through the air-soil interface, are considered and compared. The results are provided as tomographic images along the route of 1340 m; the tomographic images confirm the presence of interesting subsurface geometrical features, whose geological interpretation agrees with the studies presented in previous papers.

**Keywords** Chang'e 4, Farside of the Moon, Lunar penetrating radar, Microwave tomography

Chang'E-4 (CE-4) has represented one of the most important and fascinating missions of the Chinese Lunar Exploration Program, since it involved the first landing of a spacecraft on the far side of the Moon. CE-4 lander touched the Moon's surface on January 3, 2019 at the eastern floor of Von Kármán crater at coordinates 45.4446°S, 177.5991°E (Fig. 1a). The mission included the Yutu-2 rover equipped with a scientific payload consisting of a Panoramic Camera (PCAM), a Visible and Near-Infrared Imaging Spectrometer (VNIS), which was exploited for the identification of surface materials and atmospheric trace gases, and an Advanced Small Analyzer for Neutrals (ASAN) providing information about the interaction between the solar wind and the lunar surface. Furthermore, the Lunar Penetrating Radar (LPR) having the same features of the system already used during the Chang'e 3 mission<sup>1–3</sup> was another key instrumentation on-board the Yutu-2 rover.

CE-4 LPR is a dual-frequency time-domain GPR system, operating at the center frequencies of 60 MHz (low frequency channel) and 500 MHz (high frequency channel), with frequency bands 40–80 MHz and 250–750 MHz, respectively. In this paper, we focus on the high-frequency channel equipped with one transmitting and two receiving bowtie antennas (CH2A and CH2B). The antennas are located at the bottom of the Yutu-2 rover, approximately 0.3 m above the ground (contactless configuration), and are separated 0.16 m one from the other<sup>3</sup>.

Several results achieved by processing CE-4 LPR high frequency data are available in the literature. The LPR onboard the Yutu-2 rover firstly revealed the stratigraphy and dielectric properties of the Moon's shallow subsurface on the far side<sup>3–8</sup>. Based on radar data recorded in the first two lunar days, the shallow subsurface (<45 m) at the Chang'e-4 landing site has been divided into three distinct stratigraphic units<sup>3,6</sup>. The uppermost unit, from 0 to ~12 m, exhibits weak radar echoes with minimal electromagnetic diffraction, indicating the presence of an isotropic medium<sup>6,9</sup>. The dielectric constant and loss tangent of this layer are approximately 3.5 and 0.005, respectively, leading to its interpretation as a fine-grained regolith layer<sup>3</sup>. The second unit, from ~12 to ~24 m, exhibits more chaotic electromagnetic signals with stronger echoes compared to the fine-grained regolith, indicating a difference in the material composition. This unit is interpreted as ejecta from nearby impact craters<sup>3,6</sup>. The loss tangent of this layer is constrained to ~0.01 though its dielectric constant remains poorly constrained<sup>10</sup>. The third unit, comprising alternating ejecta layers, spans from ~24 to ~45 m, as reported in a former work<sup>3</sup>. Some studies suggest that this region might correspond to a basaltic unit<sup>4</sup>, but its dielectric constant and loss tangent have not been well constrained. In addition, by exploiting LPR data collected during

<sup>1</sup>Institute for Electromagnetic Sensing of the Environment (IREA)—National Research Council of Italy (CNR), Naples 80128, Italy. <sup>2</sup>Key Laboratory of Lunar and Deep Space Exploration, National Astronomical Observatories, Chinese Academy of Sciences, Beijing 100012, China. <sup>3</sup>University of Chinese Academy of Sciences, Beijing 100012, China. <sup>4</sup>Institute for Advanced Study, Shenzhen University, Shenzhen 518060, Guangdong, China. ✉email: soldovieri.f@irea.cnr.it

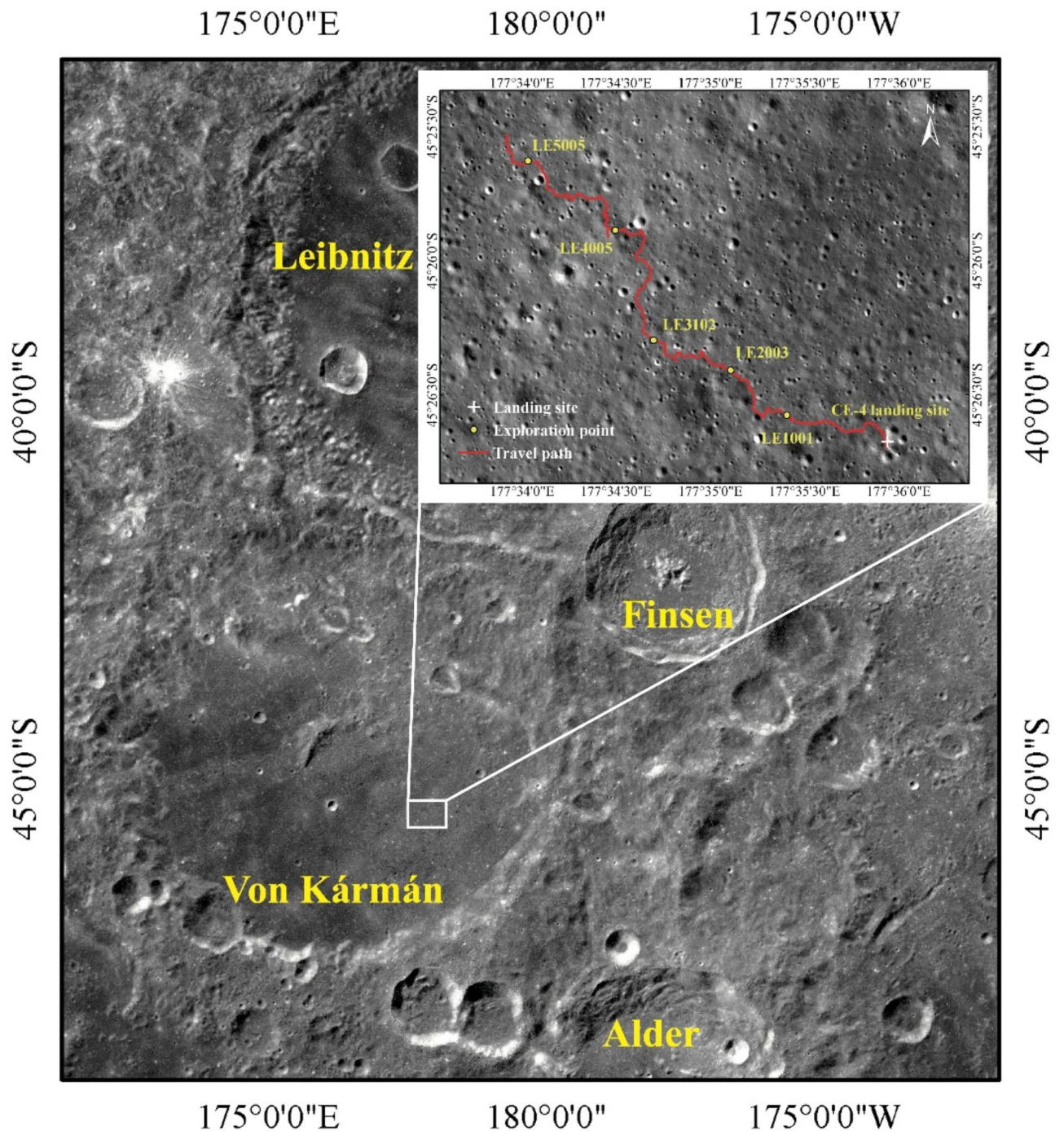


**Fig. 1.** Landing site of CE-4 mission and the route of Yutu-2 rover. **(a)** CE-4 landed in the eastern site of the Von Karman crater. The white rectangular area indicates the landing region. The basemap is CE-2 7-m resolution Digital Orthophoto Map (DOM). **(b)** Local zoom of the CE-4 landing site. The red line shows the traverse route of Yutu-2 during 53 lunar days. The basemap is Lunar Reconnaissance Orbiter Camera (LROC) image.

the first 15 lunar days, the presence of a buried crater, characterized by a rock concentrated structure, was evidenced<sup>11</sup>.

It should be noticed that the above mentioned studies are mainly based on the analysis of the LPR radargrams, which provide a representation of the scene where buried anomalies are focused only along the vertical direction but not along the direction followed by the rover. To overcome this limitation and enhance the imaging quality, a microwave tomographic imaging approach for high-frequency CE-4 LPR data has been recently exploited by the authors<sup>3</sup>.

Microwave tomography<sup>12,13</sup> is a well-assessed inversion methodology for the processing of ground penetrating radar data. The electromagnetic inverse scattering is the mathematical frame of microwave tomography, where the aim is the estimation of the geometry and electromagnetic properties of an object from the knowledge of the scattered field when an incident field impinges upon it<sup>12,13</sup>. From a mathematical viewpoint, such an inverse problem is ill-posed and non-linear<sup>12–14</sup>. Accordingly, when faced in its full non-linearity, the problem may be susceptible to false solutions that undermine the reliability of the inversion approach<sup>13</sup>. A possible strategy to face the above mentioned criticalities is the adoption of a simplified modeling of the electromagnetic scattering, which linearizes the functional relationship between the contrast function (unknown of the problem) and the scattered field data<sup>15,16</sup>. The use of this simplified model permits to solve a linear inverse problem and estimate the geometrical features of the unknown target. However, the simplification of the electromagnetic scattering modeling does not permit to achieve a quantitative image and the reconstruction performance is affected by the limited information content collected by the usual measurement configuration, which is a reflection multi-bistatic one for the LPR case at hand. A large body of literature is available regarding the estimation of the resolution limits in terms of the adopted measurement configuration and of the electromagnetic properties of the host medium (see<sup>17,18</sup> and the related bibliography). However, despite the former limitations, microwave tomographic approaches have been proven effective for subsurface imaging in several applications areas, such as cultural heritage<sup>19</sup>, civil engineering diagnostics<sup>20</sup>, through wall and indoor radar imaging<sup>21–23</sup>, and many others.

This paper addresses the application of the microwave tomographic approach for planetary exploration<sup>24</sup>. In an earlier authors' work<sup>3</sup>, a microwave tomographic approach was applied to process CE-4 LPR data collected during the first two lunar days for a rover trajectory length of about 106 m. Here, we apply microwave tomographic imaging to about 1340 m of radar data acquired by the Yutu-2 rover. Note that the original inversion approach<sup>3</sup> based on the equivalent permittivity model is herein compared to a more rigorous ray-based model<sup>18</sup> taking into account the radar signal propagation at the air-soil interface. The subsurface imaging results provided by the microwave tomographic approach are after interpreted in terms of geological features of the investigated domain also by comparing to the results already available in literature.

The paper is organized as follows. Section “Data Processing Pipeline” describes the data processing scheme and recalls the microwave tomographic approach. Tomographic imaging results are shown in Section “Experimental results”. In Section “Conclusions”, geological interpretation is provided starting from the achieved tomographic images.

## Data processing pipeline

The high-frequency radar data were collected along the whole Yutu-2 route during 53 lunar days (see Fig. 1b). The data were collected with a pulse repetition interval, i.e. the time interval between two adjacent traces, of 0.6636 s. By considering the velocity of the rover of about 5.5 cm/s, a measurement spatial step of 3.6 cm is assumed for the radargram and the tomographic imaging. The radargram collected along the overall route consists of 37.238 traces covering a traveled distance of about 1340 m. Since the first receiving antenna (CH2A) in the high-frequency system was affected by a strong cross-talk<sup>3</sup>, only the data collected by the second antenna (CH2B) are analyzed in the present work.

In the following, we present the radar data processing pipeline (see the flow chart in Fig. 2), which consists of two main stages. The first one is a standard pre-processing applied to LPR data; after, the microwave tomographic approach is applied to the data resulting by the pre-processing stage.

### A. Pre-processing

The pre-processing stage consists of the steps described below.

#### *Data reading*

LPR data collected by Yutu-2 rover are classified into 3 levels after different processing, labeled as Level 0, Level 1 and Level 2, and Level 2 data is further divided into Level 2 A, 2B, and 2 C<sup>25</sup>. Level 2B data are considered in this work. These data are produced by decoding the raw signals through several operations such as physical quantity conversion, normalization, direct current offset removal, gain removal and inclusion of geometric coordinates.

#### *Data editing*

During the LPR operation, the rover was stopped to perform other scientific tasks, causing the collection of repeated data at the same location. Accordingly, we use positioning information and perform a visual inspection of the radargram to determine whether LPR was stationary or moving during the acquisition. After, we remove the repeated data and stitch all the files together according to the collection sequence.

#### *Time-zero correction*

A time-zero correction is performed to match the zero-time with the ground (air/soil interface) location. The location of the first trough (91th sampling point corresponding to 28.4375 ns) of each trace is used as the calibration point to align all radar data<sup>25,26</sup>, so that the traces share the same zero-time position.

#### *Background subtraction*

A background subtraction is carried out to improve the signal to clutter ratio by decreasing the system ‘ring-down’ effect. The background removal is carried out segmentally according to the lunar days by calculating the mean of all traces within a section and subtracting it from each trace.

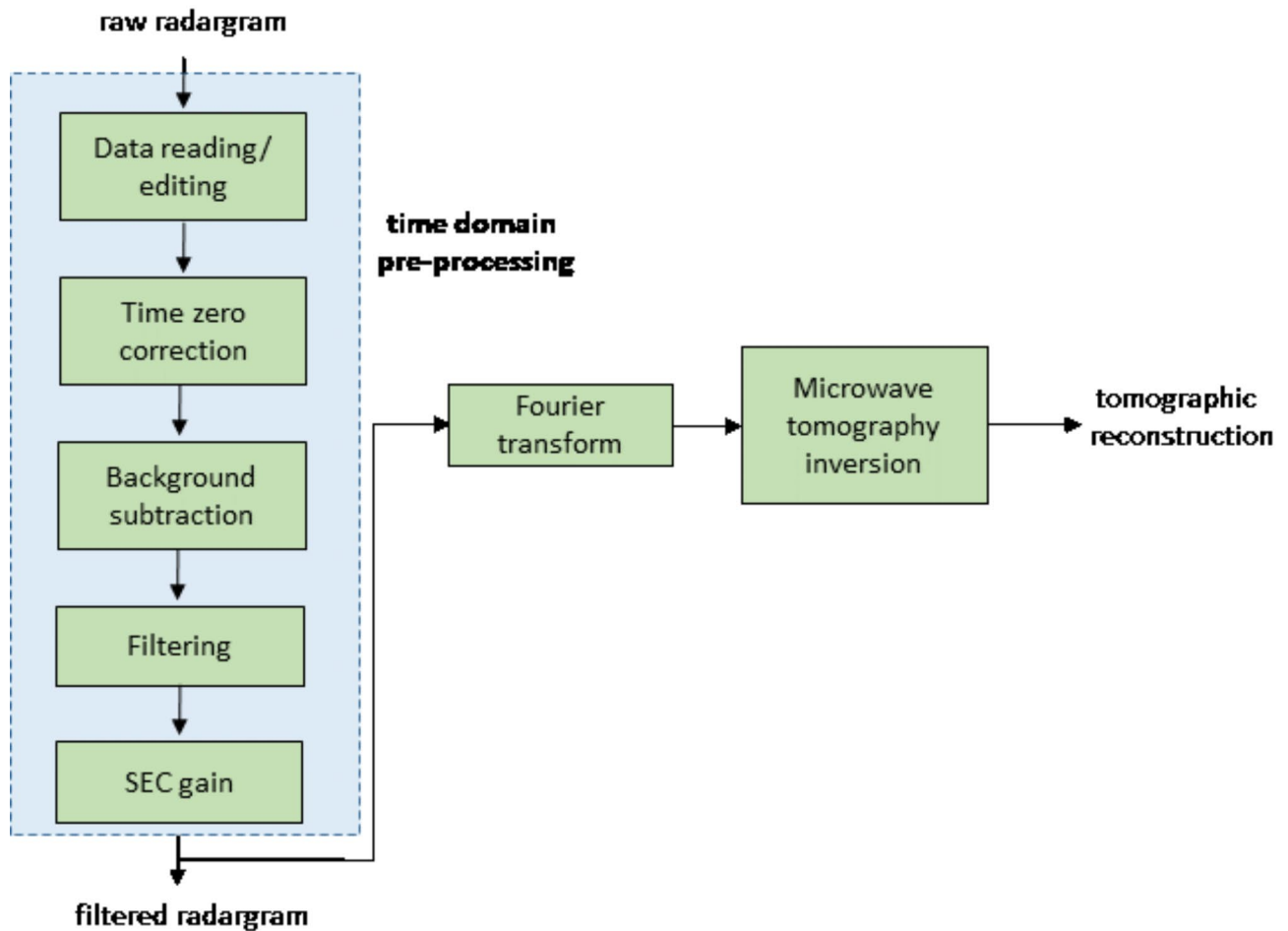


**Fig. 2.** The LPR signal processing pipeline.

#### Filtering

A Finite Impulse Response (FIR) filter with a pass range of 250–750 MHz was used for bandpass filtering to reduce noise and improve the data quality. Its low-cut frequency and high-cut frequency are set as 100 MHz and 900 MHz, respectively.

#### SEC gain

In order to further aid the visualization of the LPR sections and enhance the subsurface weak signals, a Spherical and Exponential Compensation (SEC) gain is applied. The gain function can be defined as<sup>27</sup>  $G = r^2 e^{2\alpha r}$ , where  $\alpha = \frac{\pi}{\lambda_0} \sqrt{\epsilon} \tan\delta$ ,  $r$  is the target distance, and  $\alpha$  is the attenuation constant,  $\lambda_0$  is the wavelength,  $\epsilon$  is the permittivity, and  $\tan\delta$  is the loss tangent. Here, the relative dielectric permittivity  $\epsilon$  and loss tangent  $\tan\delta$  of the lunar soil are set to 3.52 and 0.005, respectively<sup>3</sup>.

### B. Microwave tomographic approach

According to the flow chart depicted in Fig. 2, the radargram achieved after the time-domain pre-processing undergoes a Fourier Transform and finally, a microwave tomographic approach is exploited to obtain a subsurface image from which the location and the geometry of the buried targets can be estimated<sup>13,15,18</sup>. Note that here we consider two reconstruction approaches; the first one is the same previously considered for a first data set of CE-4 LPR data<sup>3</sup> based on the concept of the equivalent permittivity; the second one exploits the concept of the Interface Reflection Point (IRP)<sup>18</sup>.

The scenario considered for the tomographic inversion is the one depicted in Fig. 3, which features a two-layered medium where, the upper region ( $z < 0$ ) is free-space and the lower region ( $z > 0$ ), representing the lunar subsurface. This last is assumed for simplicity as a homogeneous, non-dispersive, and non-magnetic soil characterized by a dielectric permittivity  $\epsilon_s$ . The air-soil interface is assumed locally flat and coincident with the plane  $z=0$  of the reference system. The scene is probed by transmitting (Tx) and receiving (Rx) antennas mounted on the rover at quota  $h$ , which moves along the route  $\Gamma$ . The Tx and Rx antennas' positions are  $r_{tx}$  and  $r_{rx}$ , respectively. The antennas work in the angular frequency interval  $\Omega = [\omega_{min}, \omega_{max}]$ . Since the antennas have a fixed offset along the  $y$ -axis a multi-bistatic/multi-frequency measurement configuration is considered.

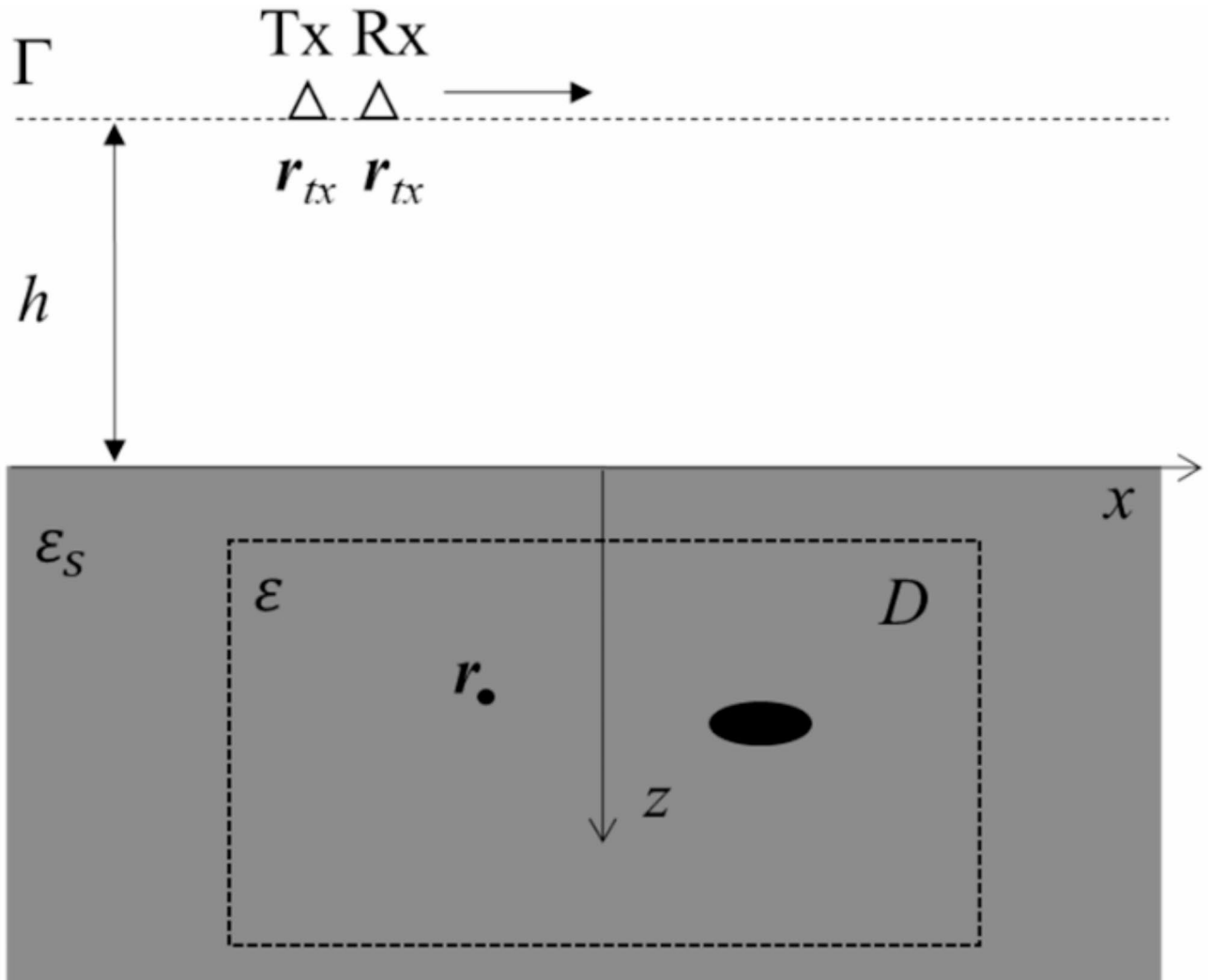


**Fig. 3.** The subsurface imaging scenario. The ellipse denotes a generic target buried in the soil.

The investigation domain  $D$ , wherein the targets are imaged, is the 2D subsurface region defined by the rover route and the depth. Moreover,  $\mathbf{r}$  is a generic point in  $D$  and  $\chi(\mathbf{r}) = \frac{\epsilon(\mathbf{r})}{\epsilon_s} - 1$  is the unknown contrast function modeling the targets in terms of the permittivity variations with respect to the soil's one. According to the simplified scalar model<sup>12,15,17</sup>, the relationship between the scattered field  $E_s$  (measured data) and the unknown contrast function  $\chi$  is given by the linear integral equation

$$E_s(\mathbf{r}_{rx}, \omega) = k_s^2 \iint_D g(\mathbf{r}_{rx}, \mathbf{r}, \omega) E_i(\mathbf{r}_{tx}, \mathbf{r}, \omega) \chi(\mathbf{r}) d\mathbf{r} = \mathcal{L}(\chi) \tag{1}$$

where  $k_s = \omega^2 \sqrt{\mu_0 \epsilon_s}$  is the propagation constant in the soil,  $g$  is the Green's function of the scenario,  $E_i$  is the incident field in  $D$ , and  $\mathcal{L}$  is the linear scattering operator mapping the unknown contrast into the scattered field data space.

The evaluation of the Green's function  $g$  and the incident field  $E_i$  (i.e. the kernel of the integral equation) implies a notable computational effort because spectral integrals have to be calculated<sup>12,18</sup> for every measurement and investigation point.

As a possible strategy to simplify the problem, an approximate model based on the *equivalent permittivity concept*<sup>18,28</sup> can be exploited. In detail, the electromagnetic wave propagation in the two-layered scenario of Fig. 3 is described as occurring into a medium with an equivalent and spatially varying dielectric permittivity. Moreover, by considering only rays propagating in the direction normal to the air-soil interface, the equivalent relative permittivity is expressed by the formula<sup>18,28</sup>

$$\epsilon_{eqs}(z) = \left( \frac{\sqrt{\epsilon_{rs}} z + h}{z + h} \right)^2 \tag{2}$$

where  $\epsilon_{rs}$  is the soil relative dielectric permittivity. Note that  $\epsilon_{eqs}$  is equal to one at the air-soil interface ( $z=0$ ) and approaches  $\epsilon_{rs}$  for large values of  $z$ .

By accounting for the reciprocity of the Green's function<sup>15</sup> and neglecting unessential amplitude factors, the integral equation in (1) is rewritten as

$$E_s(\mathbf{r}_{rx}, \omega) \approx \iint_D \frac{e^{-jk_0\sqrt{\epsilon_{eqs}(z)}R_{tx}}}{R_{tx}} \frac{e^{-jk_0\sqrt{\epsilon_{eqs}(z)}R_{rx}}}{R_{rx}} \chi(\mathbf{r}) d\mathbf{r} = \mathcal{L}(\chi) \tag{3}$$

where  $R_{tx} = |\mathbf{r}_{tx} - \mathbf{r}|$  and  $R_{rx} = |\mathbf{r}_{rx} - \mathbf{r}|$  are the distances between the generic investigation point  $\mathbf{r}$  and the Tx and Rx antenna locations, respectively.

A more refined ray-based approach is also considered in the following to enhance the accuracy in the evaluation of the kernel of the integral Eq. (1). Such an approach accounts for the actual ray propagation path from transmitting and receiving antennas to a generic point in the imaging domain. The approach, here briefly recalled for clarity, is referred to as *Interface Reflection Point (IRP)* imaging model<sup>18</sup> and is applied for the first time to LPR data processing.

As depicted in Fig. 4, the signal emitted by the TX antenna located at  $(x_m, -h)$  propagates along the incident ray, enters the soil at the IRP  $(x_r, 0)$ , and finally reaches the target point at  $(x, z)$ . The IRP depends on both the source and target points and can be determined using Snell's law of refraction:

$$\sin(\theta^i) = \frac{x_r - x_m}{R_1} = \sqrt{\epsilon_{rs}} \sin(\theta^t) = \sqrt{\epsilon_{rs}} \frac{x - x_r}{R_2} \tag{4}$$

where  $\theta^i$  and  $\theta^t$  are the incidence and transmission angles relative to the normal of the air-soil interface,  $R_1 = \sqrt{(x_r - x_m)^2 + h^2}$  and  $R_2 = \sqrt{(x - x_r)^2 + z^2}$  are the path lengths along incident and transmitted rays (see Fig. 4). Equation (4) results in a fourth-order polynomial with respect to the unknown  $x_r$ . This equation can be solved numerically, considering only the root that satisfies  $x_r \leq x$ , if  $x \geq x_m$  or  $x_r \geq x$ , if  $x \leq x_m$ .

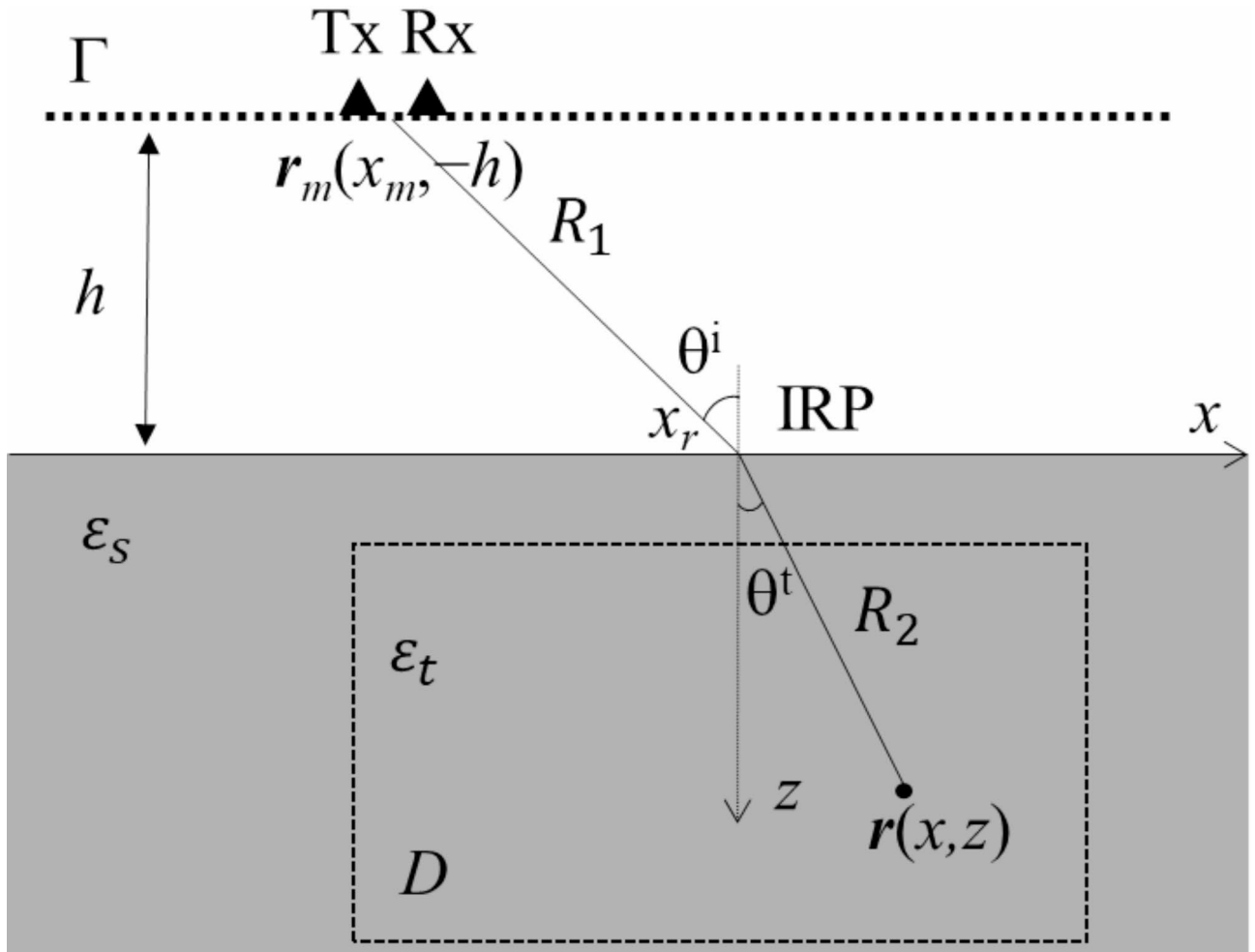


Fig. 4. Geometry relevant to the IRP model.

Once the IRP is computed,  $g$  and  $E_i$  are determined using geometrical optics principles. Subsequently, the linear integral Eq. (1) to be inverted is expressed as:

$$E_s(\mathbf{r}_m, \omega) \approx \iint_D \frac{e^{-j2k_0(R_1 + \sqrt{\epsilon_{rs}} R_2)}}{R_1 + R_2} \chi(\mathbf{r}) d\mathbf{r} \tag{5}$$

The linear inverse problem in Eqs. (3) and (5) is ill-posed and a regularized scheme is required to obtain a stable solution<sup>14</sup>. In this work, the adjoint inversion scheme<sup>16</sup> is applied to solve the inverse problem

$$\tilde{\chi}(\mathbf{r}) = \mathcal{L}^+ E_s \tag{6}$$

where  $\mathcal{L}^+$  is the adjoint operator of  $\mathcal{L}$ .

The modulus of the regularized contrast  $\tilde{\chi}$  in Eq. (6) is a spatial map denoted as tomographic image. It must be stressed that such an image is a qualitative map providing information on the presence, location, and approximate shape of the targets. More specifically, the location and geometry of the buried targets is identified as the areas in the investigation domain  $D$ , where the amplitude of the contrast function is not negligible.

It must be stressed that the IRP model is in principle more accurate compared to the equivalent permittivity one because it describes more accurately the phase of the incident field in the investigation domain. On the other hand, IRP inversion model is characterized by a slightly larger computational burden because the IRP needs to be evaluated for any measurement and investigation point<sup>18</sup>. This additional computation burden can be tolerated since the evaluation of the kernel of the relevant integral equation under IRP model is performed only one time for fixed processing parameters.

Before proceeding further, it must be stressed that the computation of the operator  $\mathcal{L}^+$  is not feasible in the case of very large (in terms of probing wavelength) measurement and observation domains, as this would demand huge computation resources. To overcome this drawback, we apply the shifting zoom approach for data inversion<sup>29,30</sup>. The approach consists in the following steps that are described with the aid of Fig. 5:

1. the investigation domain  $D$  is split into  $N$  subdomains  $D_n, n=1, \dots, N$ , such that  $D = \cup_{n=1}^N D_n$ ;
2. for each subdomain  $D_n$ , only radar traces falling into measurement window  $\Gamma_n, n=1, \dots, N$ , are considered for the imaging. The window  $\Gamma_n$  are chosen symmetrical along  $x$ -axis with respect to the center of each subdomain  $D_n$ ;

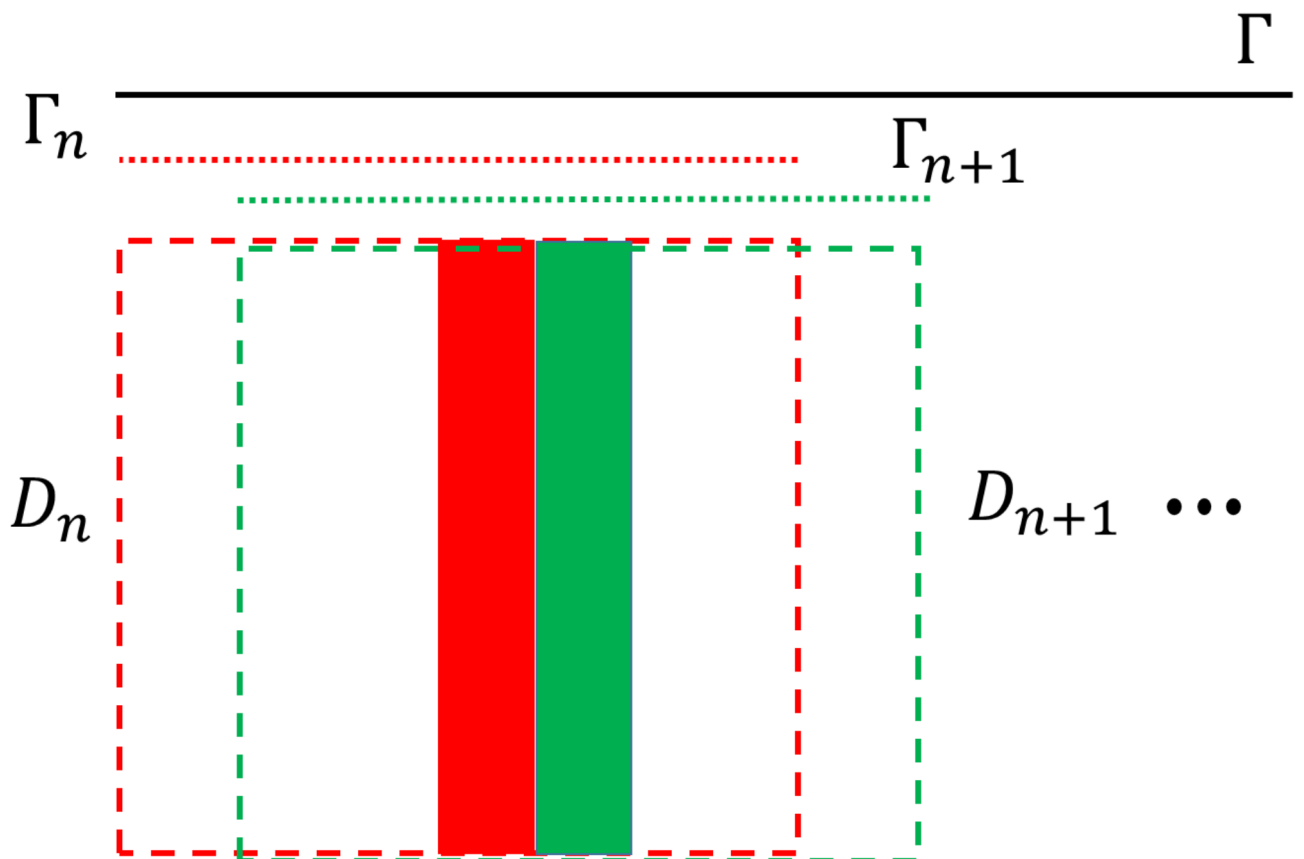


Fig. 5. The shifting zoom concept.

3. a tomographic image  $\tilde{\chi}_n$  is obtained by adjoint inversion (see Eq. (6)) for each subdomain  $D_n$ ;
4. the tomographic image of the whole scene  $D$  (along the overall rover route) is obtained by the superposition of the central belts of the reconstructions  $\tilde{\chi}_n$  achieved at the step 3) according to<sup>29,30</sup>.

The main feature of shifting zoom approach is the possibility to process a large amount of data by inverting a sequence of small datasets, where each of them provides information of a smaller region of the overall investigated area. Moreover, a notable saving of computation time and resources is achieved by choosing equal size subdomains  $D_n$  such that the adjoint operator  $\mathcal{L}^+$  has to be computed only one time.

The choice of the sliding window in the shifting zoom approach is carried out empirically. In principle a larger window size yields a better resolution along the measurement direction when imaging localized scatterers. However, a larger window also implies a higher computation burden both in terms of memory requirements and processing time.

The microwave tomographic data processing is performed under MATLAB 2022 environment on a standard laptop equipped with an Intel(R) Core(TM) i7-8565U CPU @ 1.80 GHz and 16 GB RAM. The tomographic data processing takes about 24 min with both equivalent permittivity and IRP inversion strategies. However, the IRP strategy needs an additional time of about 21 s for the IRP evaluation.

## Experimental results

The collected data are processed according to the flowchart described in the Section “Data Processing Pipeline”. For the analysis presented in this paper, the background relative dielectric permittivity is chosen equal to 3.52, which is the same value considered in a previous work<sup>3</sup>. We consider a maximum depth of investigation of 48 m corresponding to a fast-time window of 600 ns. The nominal working frequency band 250–750 MHz, with a step of 1.5 MHz, is assumed in the tomographic inversion. According to chosen frequency bandwidth and having assumed a relative background permittivity of 3.52, we have a nominal vertical resolution of 0.16 m. The extent of the measurement aperture  $\Gamma_n$  in the shifting zoom approach is equal to 12.5 m. As said above, this value is set empirically even if no visible changes in the reconstructions have been observed for window sizes in the range 10–15 m. Moreover, the hypothesis of a flat air-soil interface within the shifting zoom measurement window is reasonable because the surface topography variations with respect to the flatness are small compared to the probing wavelength.

The tomographic reconstruction is given in terms of the amplitude of the contrast function normalized to its maximum along the overall rover’s route. Figure 6 provides a comparison between the B-scan after time-domain pre-processing (Fig. 6a) and the tomographic images along the overall rover’s route obtained with the equivalent permittivity model (Fig. 6b) and the IRP model (Fig. 6c). This figure aims at demonstrating the consistency between the radargram and the tomographic images. Notably, the comparison between the tomographic reconstructions highlights that very similar results are achieved with both inversion strategies corroborating the validity of applying the approximate equivalent permittivity model. The significant similarity of the two results is even better evidenced by the comparison of the reconstructions along the first 100 m of the route (see Fig. 7). Of course, equally good comparisons are obtained also in other parts of the route. Therefore, in the rest of the paper, it is implicitly assumed that the tomographic images are obtained by inverting the equivalent permittivity model.

An easier interpretation of the tomographic results can be achieved by analyzing the reconstructions plotted in Fig. 8, where the images are shown in the right spatial scale over adjacent investigation domains each one approximately 268 m long.

First, in the initial part of the route up to about 140 m (Fig. 8a), we observe a layered structure with clearly distinguishable interfaces. After, as seen in Fig. 8b and d, we detect the presence of two interfaces at a depth of about 20 m and 30 m, respectively, in the interval between about  $x=380$  m to about  $x=800$  m. The presence of a depression is also evident with its two boundaries detected in Fig. 7b at about  $x=400$  m and in Fig. 8d at about  $x=950$  m, respectively. These boundaries go slowly in depth starting from few meters to about 15 m.

The two interfaces observed up to  $x=900$  m are followed by a sloping strip rocky blocks from  $x=900$  m to  $x=1000$  m, followed again by two interfaces at depth of 20 m and 25 m. Another interesting feature occurs in the approximate range 1000–1100 m, where an undulating interface at about 15 m of depth is above a deeper interface at about 25 m, after which a region characterized by rocky blocks is observed. In the final part of the domain, after about  $x=1100$  m, interfaces are missing and the region is characterized by rocky blocks, which after about  $x=1220$  m produces a lower scattering compared to the other areas.

Finally, another interesting feature regards the presence of buried lens structures, characterized by a homogeneous material, see for example the feature from  $x=35$  m to  $x=80$  m at the depth of about 30 m. Similar structures can be detected in the initial part of the investigated area (see panels 8a and 8b).

The tomographic image is interpreted in Fig. 9a and reveals a more detailed stratigraphy within the upper ~40 m of the landing area, dividing it into four main geological units as also reported in the pictorial representation of Fig. 9b. The interpretation of subsurface stratigraphy using GPR radar is primarily based on the dielectric properties calculated for each layer. The first unit (Unit 1), with a thickness of ~12 m to 18 m, is consistent with some previous studies<sup>3,6,31</sup>, and it is interpreted as well-weathered fine-grained regolith because its dielectric constant is calculated to be ~3.5 to 4. This layer is commonly thought to originate from the weathering of ejecta from the Finsen crater<sup>29</sup>. The second unit (Unit 2), extending from ~12 m to ~30 m, contains chaotic electromagnetic echoes, indicating multiple reflectors within the medium. This layer is interpreted as unweathered impact ejecta, typically consisting of a mixture of fragmented rocks and regolith, with inclusions of remnants from other impact craters. This interpretation is supported by the loss tangent of ~0.01, consistent with the dielectric properties of typical ejecta<sup>32</sup>. Additionally, the radar echoes within this unit reveal multiple scattering bodies, further reinforcing its identification as ejecta. The third unit (Unit 3), located

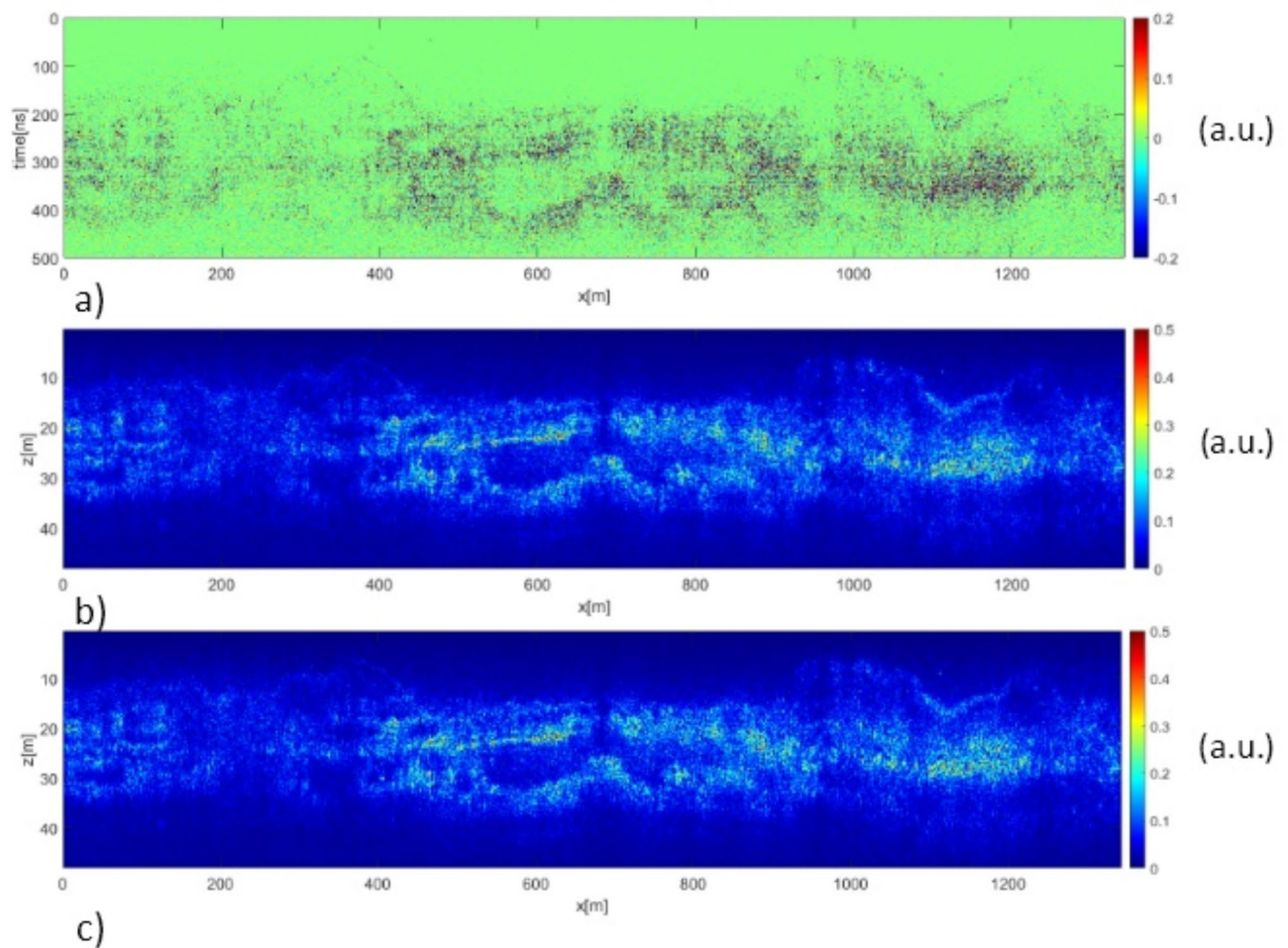


**Fig. 6.** (a) The pre-processed radargram. (b) Tomographic reconstruction obtained with the equivalent permittivity model along the overall route. c) Tomographic reconstruction obtained with the IRP model along the overall route. The color scale is expressed in arbitrary units (a.u.).

between  $\sim 27$  m and  $\sim 32$  m, contains a buried structure with a dielectric constant of  $\sim 10.5$  and a loss tangent of  $\sim 0.037$  according to a recent study by Ding et al.<sup>33</sup>. These values are characteristic of dense basalt, contradicting the previous interpretation, which identified this layer as fine-grained lunar regolith<sup>3</sup>. Laterally, this unit also shows uniform internal echoes between  $x = 300$  m and  $x = 900$  m. A subsequent work<sup>31</sup> supported findings by Ding et al. through a two-dimensional time-frequency analysis of radar imaging down to  $\sim 40$  m. Finally, the fourth unit (Unit 4), extending from  $\sim 32$  m to the noise floor at  $\sim 40$  m, exhibits more chaotic radar signatures similar to those of the second unit, suggesting that it is also composed of impact ejecta. However, there is no literature providing dielectric permittivity estimation for this unit. Its interpretation is primarily inferred from the radar echo characteristics and reasonable deductions based on the local geological context.

Finally, Fig. 10 displays the tomographic image where the effect of surface topography is compensated. As observed before, local topography variations within the SZ window are negligible as well as the changes along the overall route provided by the altimeter equal to about 11 m peak-to-peak variation on 1340 m route length.

## Conclusions

By exploiting the microwave tomographic approach, we processed 1340 m of radar data recently acquired by the Change-4 rover, generating high-resolution images of the lunar subsurface down to  $\sim 40$  m. Specifically, two imaging approaches based on the equivalent permittivity model and the interface reflection point have been considered and shown to provide comparable results. The tomographic reconstructions provide significant insights into subsurface stratigraphy. Based on the processed data and previous estimates of the dielectric properties, we have identified four distinct stratigraphic layers: a fine-grained lunar regolith layer consistent with typical lunar regolith properties; an ejecta layer with radar echoes showing multiple scattering bodies indicative of impact origin; a dense basalt layer with properties characteristic of typical basalt, differing from earlier interpretations; and an underlying ejecta layer exhibiting chaotic radar echoes similar to the second layer, suggesting a similar impact-related origin. This approach significantly enhances the interpretative quality of radar imaging, offering precise insights into subsurface stratigraphy while demonstrating strong potential for

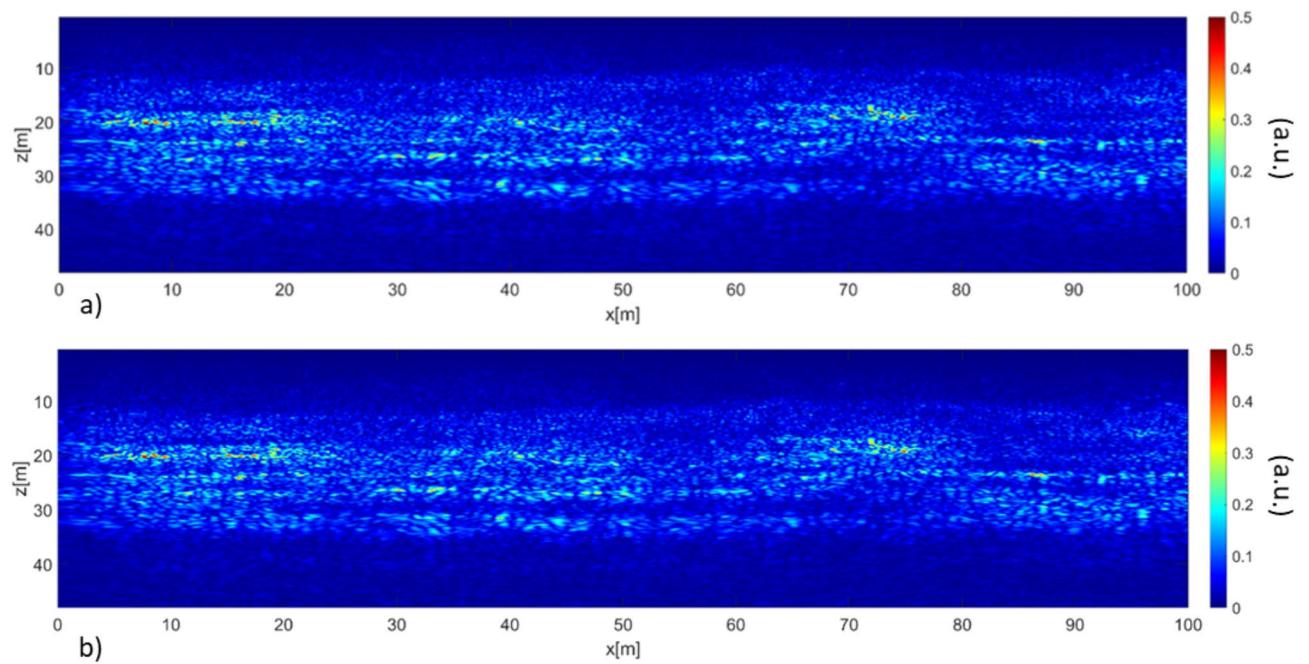


**Fig. 7.** Tomographic reconstruction obtained along the first 100 m of the route. (a) equivalent permittivity model. (b) IRP model. The color scale is expressed in arbitrary units (a.u.).

application to ground-penetrating radar data from other celestial bodies, thereby supporting future planetary exploration missions. As further developments, we aim at considering a more complicated scenario, where the subsurface layering is taken into account in the inversion model (as background scenario), with the end to better characterize the scatterers inside the single layers.

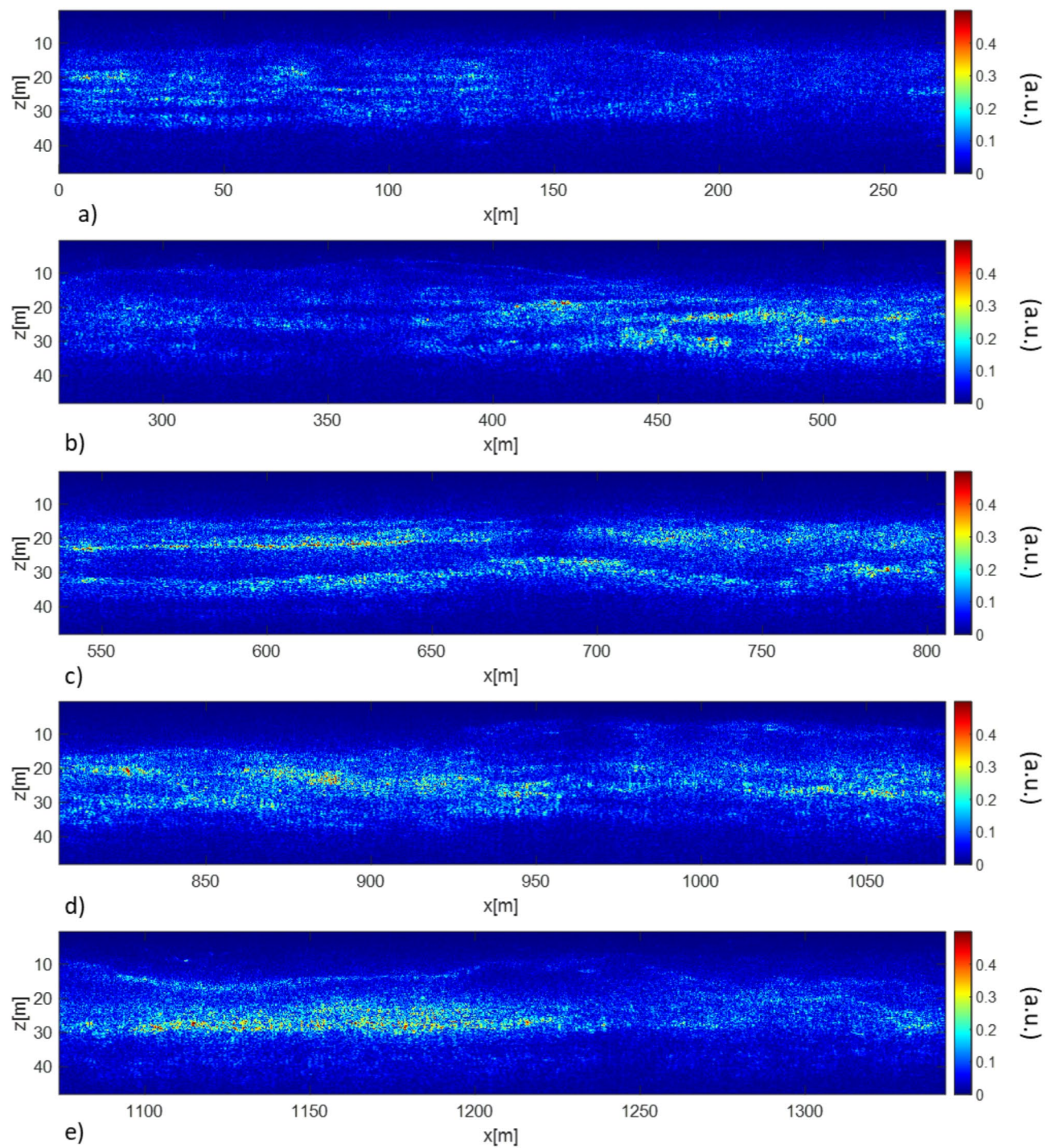


**Fig. 8.** Zoom of the tomographic reconstruction over intervals wide about 268 m. The color scale is expressed in arbitrary units (a.u.).

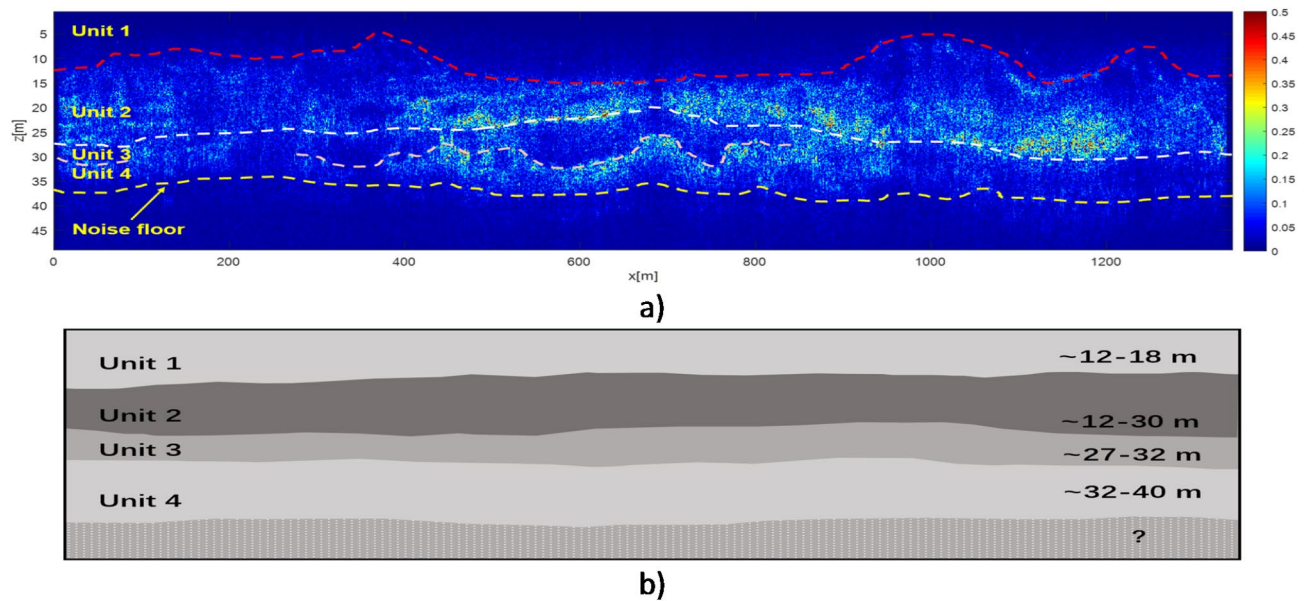


**Fig. 9.** (a) Geological Interpretation of Chang'e-4 High-Frequency Radar Data. (b) Pictorial representation of the layered subsurface.

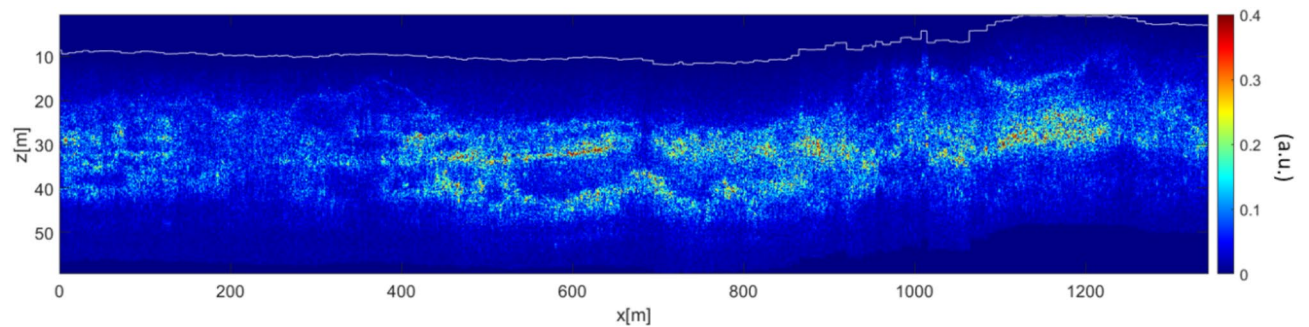


**Fig. 10.** Tomographic image along the overall route with topography correction.

### Data availability

The datasets used and/or analyzed during the current study are available at [https://clpds.bao.ac.cn/ce5web/searchOrder\\_dataSearchData.search](https://clpds.bao.ac.cn/ce5web/searchOrder_dataSearchData.search).

Received: 26 August 2024; Accepted: 7 February 2025

Published online: 12 February 2025

### References

- Fang, G. et al. Lunar penetrating radar onboard the Chang'e-3 mission. *Res. Astron. Astrophys.* **14**, 1607–1622 (2014).
- Wu, W. et al. Lunar Farside to be explored by Chang'e-4. *Nat. Geosci.* **12**, 222–223 (2019).
- Li, C. et al. The Moon's farside shallow subsurface structure unveiled by Chang'E-4 Lunar Penetrating Radar. *Sci. Adv.* **6**, 6898 (2020).
- Lai, J. et al. Comparison of dielectric properties and structure of lunar regolith at Chang'e-3 and Chang'e-4 landing sites revealed by ground-penetrating radar. *Geophys. Res. Lett.* **46**, 12783–12793 (2019).
- Roncoroni, G. et al. Deep learning driven interpretation of Chang'E-4 Lunar Penetrating Radar. *Icarus* **421**, 116219 (2024).
- Zhang, J. H. et al. Lunar regolith and substructure at Chang'E-4 landing site in South Pole-Aitken basin. *Nat. Astronomy.* **5**, 25–30 (2021).
- Zhang, L. et al. Stratigraphy of the Von Karman Crater Based on Chang'E-4 Lunar Penetrating Radar Data. *Geophys. Res. Lett.*, **47**, 1–8 (2020).
- Ding, C. et al. Yutu-2 radar observation of the lunar regolith heterogeneity at the Chang'E-4 landing site. *Astron. Astrophys.* **664**, A43 (2022).
- Ding, C. Y. et al. Fragments delivered by secondary craters at the Chang'E-4 landing site. *Geophys. Res. Lett.*, **47**, 1–9 (2020).
- Lai, J. et al. Dielectric properties of lunar materials at the Chang'e-4 landing site. *Remote Sens.* **13**, 4056 (2021).
- Zhou, H. et al. Yutu-2 radar sounding evidence of a buried crater at Chang'E-4 landing site. *IEEE Trans. Geosci. Remote Sens.* **60**, 1–19 (2021).
- Persico, R. *Introduction to Ground Penetrating Radar: Inverse Scattering and data Processing* (Wiley, 2014).

13. Pastorino, M. & Randazzo, A. *Microwave Imaging Methods and Applications* (Artech House, 2018).
14. Bertero, M., Boccacci, P. & De Mol, C. *Introduction to Inverse Problems in Imaging* (CRC, 2021).
15. Chew, W. C. *Waves and Fields in Inhomogeneous Media* (Wiley, 1999).
16. Solimene, R. et al. Imaging algorithms and some unconventional applications: a unified mathematical overview. *IEEE Signal Process. Mag.* **31**, 90–98 (2014).
17. Persico, R., Bernini, R. & Soldovieri, F. The role of the measurement configuration in inverse scattering from buried objects under the born approximation. *IEEE Trans. Antennas Propag.* **53**, 1875–1887 (2005).
18. Catapano, I. et al. Contactless ground penetrating radar imaging: state of the art, challenges, and microwave tomography-based data processing. *IEEE Geoscience Remote Sens. Magazine.* **10**, 251–273 (2022).
19. Catapano, I. et al. Applying ground-penetrating radar and microwave tomography data processing in cultural heritage: state of the art and future trends. *IEEE Signal Process. Mag.* **36**, 53–61 (2019).
20. Hugenschmidt, J. et al. Processing strategies for high-resolution GPR concrete inspections. *NDT E International.* **43**, 334–342 (2010).
21. Soldovieri, F. & Solimene, R. Through-wall imaging via a linear inverse scattering algorithm. *IEEE Geosci. Remote Sens. Lett.* **4**, 513–517 (2007).
22. Zhang, W. & Hoorfar, A. Three-dimensional real-time through-the-wall radar imaging with diffraction tomographic algorithm. *IEEE Trans. Geosci. Remote Sens.* **51**, 4155–4163 (2012).
23. Gennarelli, G. et al. Passive multiarray image fusion for RF tomography by opportunistic sources. *IEEE Geosci. Remote Sens. Lett.* **12**, 641–645 (2014).
24. Soldovieri, F., Prisco, G. & Hamran, S. E. A preparatory study on subsurface exploration on Mars using GPR and microwave tomography. *Planet. Space Sci.* **57**, 1076–1084 (2009).
25. Su, Y. et al. Data processing and initial results of Chang'e-3 lunar penetrating radar. *Res. Astron. Astrophys.* **14**, 1623 (2014).
26. Feng, J. Dielectric properties estimation of the lunar regolith at CE-3 landing site using lunar penetrating radar data. *Icarus* **284**, 424–430 (2017).
27. Feng, J. et al. Layered structures in the upper several hundred meters of the Moon along the Chang'E-4 rover's first 1,000-m traverse. *J. Geophys. Research: Planet.* **128** (e2022JE007714), 1–11 (2023).
28. Gennarelli, G. et al. A ground penetrating radar imaging approach for a heterogeneous subsoil with a vertical permittivity gradient. *IEEE Trans. Geosci. Remote Sens.* **59**, 5698–5710 (2021).
29. Persico, R. et al. Two-dimensional linear inversion of GPR data with a shifting zoom along the observation line. *Remote Sens.* **9**, 980 (2017).
30. Persico, R. et al. Improvement of ground penetrating radar (GPR) data interpretability by an enhanced inverse scattering strategy. *Surv. Geophys.* **39**, 1069–1079 (2018).
31. Giannakis, I. et al. Evidence of shallow basaltic lava layers in Von Kármán crater from Yutu-2 Lunar Penetrating Radar. *Icarus* **408**, 115837 (2024).
32. Lai, J., Cui, F., Xu, Y., Liu, C. & Zhang, L. Dielectric properties of lunar materials at the Chang'e-4 landing site. *Remote Sens.* **13**, 4056 (2021).
33. Ding, C., Li, J. & Hu, R. Moon-based ground-penetrating radar observation of the latest volcanic activity at the Chang'E-4 landing site. *IEEE Trans. Geosci. Remote Sens.* **61**, 1–10 (2023).

## Acknowledgments

This work was supported by the Research Project PRIN2022-Modeling and Deep Learning in Inverse Scattering Problems: A New Paradigm under Grant 2022T3FHLH.

## Author contributions

F.S. organized and wrote the manuscript, and developed and applied the tomographic imaging approach. G.G. wrote the manuscript and developed and applied the tomographic imaging approach. C.D. performed the data interpretation. W.D. performed data processing and landing area imaging. Y.S. organized and wrote the manuscript, and performed the data processing.

## Declarations

## Competing interests

The authors declare no competing interests.

## Additional information

**Correspondence** and requests for materials should be addressed to F.S.

**Reprints and permissions information** is available at [www.nature.com/reprints](http://www.nature.com/reprints).

**Publisher's note** Springer Nature remains neutral with regard to jurisdictional claims in published maps and institutional affiliations.

**Open Access** This article is licensed under a Creative Commons Attribution-NonCommercial-NoDerivatives 4.0 International License, which permits any non-commercial use, sharing, distribution and reproduction in any medium or format, as long as you give appropriate credit to the original author(s) and the source, provide a link to the Creative Commons licence, and indicate if you modified the licensed material. You do not have permission under this licence to share adapted material derived from this article or parts of it. The images or other third party material in this article are included in the article's Creative Commons licence, unless indicated otherwise in a credit line to the material. If material is not included in the article's Creative Commons licence and your intended use is not permitted by statutory regulation or exceeds the permitted use, you will need to obtain permission directly from the copyright holder. To view a copy of this licence, visit <http://creativecommons.org/licenses/by-nc-nd/4.0/>.

© The Author(s) 2025